

Notice: This manuscript has been authored by UT-Battelle, LLC, under Contract No. DE-AC0500OR22725 with the U.S. Department of Energy. The United States Government retains and the publisher, by accepting the article for publication, acknowledges that the United States Government retains a non-exclusive, paid-up, irrevocable, world-wide license to publish or reproduce the published form of this manuscript, or allow others to do so, for the United States Government purposes. The Department of Energy will provide public access to these results of federally sponsored research in accordance with the DOE Public Access Plan (<http://energy.gov/downloads/doe-public-access-plan>).

Electron-beam induced emergence of mesoscopic ordering in layered MnPS₃

Kevin M. Roccapriore,^{1*} Nan Huang,² Mark P. Oxley,¹ Vinit Sharma,^{4,5} Timothy Taylor,⁶ Swagata Acharya,⁷ Dimitar Pashov,⁸ Mikhail I. Katsnelson,⁷ David Mandrus,^{2,3} Janice L. Musfeldt,^{6,9} and Sergei V. Kalinin^{1*}

¹ The Center for Nanophase Materials Sciences Oak Ridge National Laboratory, Oak Ridge, TN 37831

² Department of Materials Science and Engineering, University of Tennessee, Knoxville TN, 37916

³ Materials Science and Technology Division, Oak Ridge National Laboratory, Oak Ridge, TN 37831

⁴ Computational Sciences Division Oak Ridge National Laboratory, Oak Ridge, TN 37831

⁵ National Institute for Computational Sciences, University of Tennessee, Knoxville TN, 37831

⁶ Department of Chemistry, University of Tennessee, Knoxville, Tennessee 37996, USA

⁷ Institute for Molecules and Materials, Radboud University, NL-6525 AJ Nijmegen, The Netherlands

⁸ King's College London, Theory and Simulation of Condensed Matter, The Strand, WC2R 2LS London, UK

⁹ Department of Physics and Astronomy, University of Tennessee, Knoxville, Tennessee 37996, USA

Ordered mesoscale structures in 2D materials induced by small misorientations have opened pathways for a wide variety of novel electronic, ferroelectric, and quantum phenomena. Until now, the only mechanism to induce this periodic ordering was via mechanical rotations between the layers, with the periodicity of the resulting moiré pattern being directly related to twist angle. Here we report a fundamentally new mechanism for emergence of mesoscopic periodic patterns in multilayer sulfur-containing metal phosphorous trichalcogenide, MnPS₃, induced by the electron beam. The formation under the beam of periodic hexagonal patterns with several characteristic length scales, nucleation and transitions between the phases, and local dynamics are demonstrated. The associated mechanisms are attributed to the relative contraction of the layers caused by beam-induced sulphur vacancy formation with subsequent ordering and lattice parameter change. As a

* roccapriorkm@ornl.gov

* sergei2@ornl.gov

result, the plasmonic response of the system is locally altered, suggesting an element of control over plasmon resonances by electron beam patterning. We pose that harnessing this phenomenon provides both insight into fundamental physics of quantum materials and opens a pathway towards device applications by enabling controlled periodic potentials on the atomic scale.

Over the last 15 years, two-dimensional materials including graphene, boron nitride, and transition metal dichalcogenides have propelled to the forefront of scientific research due to a unique combination of structural, electronic, and quantum properties they offer. Shrinking the dimensionality of a bulk crystal down to two dimensions invariably leads to unconventional physics by imposing confinement effects, creating anomalous structural configurations, and enabling the emergence of unusual electronic structure. Owing to the incredible ease of preparing a few or even a single layer of atoms, many two-dimensional materials offer a superb platform to rapidly conduct an enormous variety of experiments.

While the initial progress was based preponderantly on device-level measurements, advances in scanning transmission electron microscopy (STEM) have ushered a new era in understanding local structural, electronic, and even vibrational properties of materials at the atomic scale. The structure, property, and dynamic of individual point defects, defect complexes, and grain boundaries have been extensively explored via aberration-corrected structural imaging. The development of monochromated¹ high resolution electron energy loss spectroscopy has enabled direct mapping of plasmons and excitons in these materials.² The 4D-STEM techniques³ have enabled high precision structural mapping,⁴ opening the pathway towards exploration of strain and symmetry breaking phenomena,⁵ as well probing the detailed 3D structure of defects. Finally, the potential of the electron beam to induce controllable chemical changes has been harnessed to create controlled edges,⁶ atomically-defined nanopores and device structures,⁷ and even controllably move individual dopant atoms and assemble homo- and heteroatomic artificial molecules.^{8,9}

Over the last three years, the field has developed the new impetus with the discovery of a wealth of novel phenomena in twisted van der Waals heterostructures.¹⁰ Here, the discovery of superconductivity in twisted bilayer graphene^{11,12} and more recently twisted trilayer graphene^{13,14} has sparked a wave of interest in these materials. Immediately afterwards was the realization that ferroelectricity is also possible within the twisted material paradigm in graphene and boron nitride.¹⁵ Similarly, STEM has offered a new set of insights into atomistic mechanisms, demonstrating the presence of topological defects that may give rise to effects such as second harmonic generation, strain solitons, and adsorption enhancement.^{16–18} Jointly, these developments have seeded the field of twistronics and have significantly exploited the functionalities and behaviors manifest in 2D materials, further enabling a broad set of device-relevant applications.

However, this broad variety of emergent functionalities is ultimately derived based on the mechanical rotation of two or more layers with respect to each other. This constraint both necessitates complex fabrication routines and renders the average rotation angle a conserved parameter. While topological defects and ferroelectric domains can be manipulated, the background rotation angle cannot. Hence, of significant interest is the development of mesoscopic ordered structures allowing for control of local potential.

Here, we report the emergence of periodically ordered structures and their manipulation using the electron beam in MnPS₃, a lesser studied complex van der Waals material. This material belongs to the family of metal phosphorous trichalcogenides,^{19,20} and has been considered as a potential candidate material with unique 2D magnetic ordering. Similar to many 2D materials, MnPS₃ can be easily exfoliated to yield flakes of single or several layers. These to our knowledge

have only recently begun to be explored for possible functionalities of interest, however comparison with other metal phosphorous trichalcogenides suggest potential emergence of ferro- and antiferroelectric behavior, ionic conduction, and other functionalities. Similarly, this material can serve as a host for cationic substitution on the metal site, and anion substitution on the chalcogen site. Curiously, the electronic properties of bulk and single and few layers were investigated by EELS but with parallel illumination in the TEM,^{21,22} but no lattice compression or otherwise peculiar structural findings were noted. The antiferromagnetic transition has been studied by STM²³, Raman spectroscopy,^{24,25} and tunneling magnetoresistance measurements²⁶ as long as fifty years ago. Aside from magnetism approaching the two-dimensional limit, MnPS₃ has also been considered a candidate for transistors, UV photodetectors,²⁷ NO₂ gas sensing,²⁸ and battery electrodes with Li intercalation.²⁹ More recently, the vibrational properties of MnPS₃ were studied with near-field infrared spectroscopy where layer-dependent symmetry crossovers were realized.^{30,31} MnPS₃ also was found to display piezochromism.³²

It is important to mention that many of the compounds in the metal phosphorous trichalcogenide family are notorious for being beam sensitive to STEM imaging, presumably due to sulfur being easily removed at a variety of accelerating voltages, primarily a result of knock-on damage or radiolysis.^{33,34} In fact, the recent availability of low acceleration voltage STEM enabled by aberration corrections was in part the motivation behind this study.

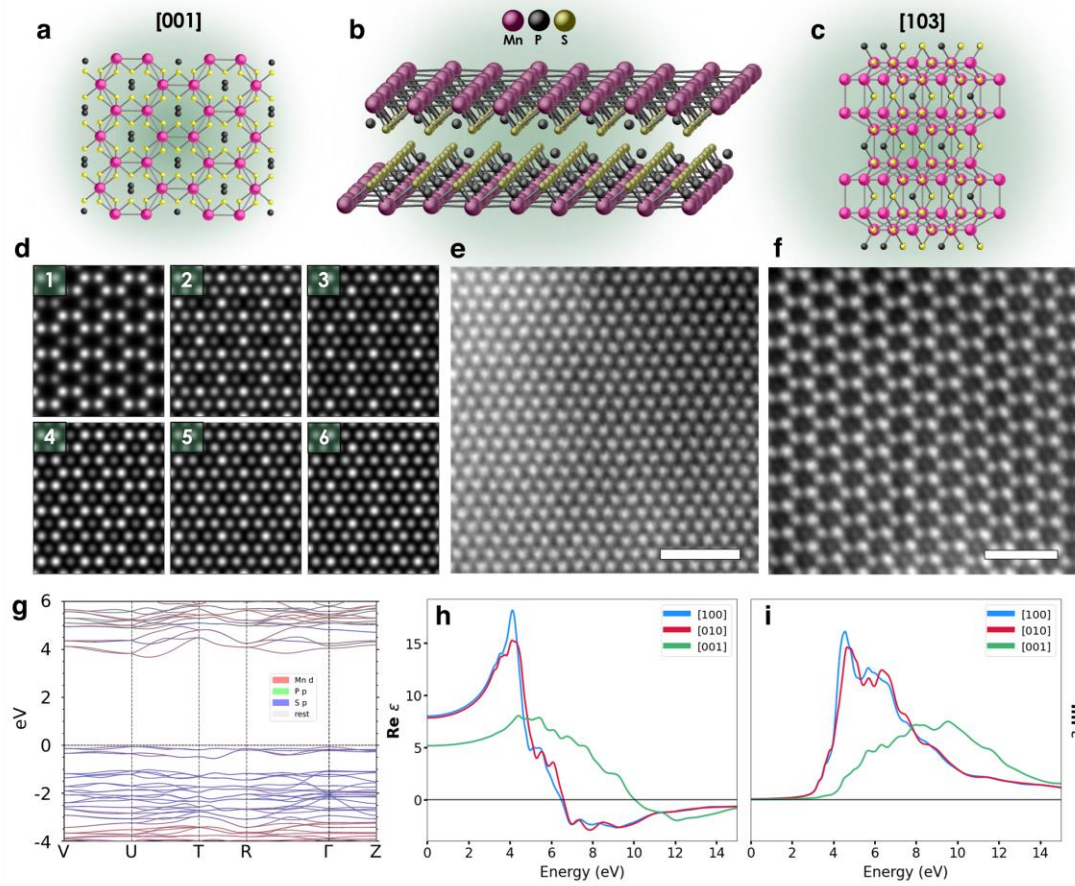


Figure 1. MnPS₃ structure and electronic properties. Two selected orientations shown in **a** and **c** with 3D view in **b**. Multislice image simulations for one through six atomic layers shown in **d**, and HAADF-STEM images viewed in [103] projection in **e** for several layers and in **f** for near single layer. Electronic band structure (QSGW) calculation (**g**) and calculated real (**h**) and imaginary (**i**) parts of electron-hole vertex corrected macroscopic dielectric function for electric field applied along three different crystal axis directions. Scalebars in **e** and **f** are 1 nm.

Single crystals of MnPS₃ were synthesized through the chemical vapor transport method³⁵ with a detailed description in the Methods section. Sheets of MnPS₃ were directly exfoliated to TEM grids using thermal release tape, omitting a transfer step in order to avoid chemical residues and simplify the process. The crystal structure of MnPS₃ is shown in a few different orientations in **Figure 1**. Due to the relative shift of the layers as seen in Figure 1**b**, the [103] orientation is the most natural viewing orientation after cleaving, with the plane of Mn atoms orthogonal to the beam axis. STEM image simulations were performed using the μ STEM package³⁶ in the same zone axis, and reveal an abundance of atomic contrast variations depending on number of atomic layers,

helping to aid in determining specimen thickness. Visualization of the atomic structure is achieved with aberration corrected HAADF-STEM imaging at 60 kV, where panels **e** and **f** in Figure 1 show the stark difference between only a few layers. In this projection, two of the three elements are simultaneously present in each atomic column – either S and Mn or S and P – enabling a variety of contrast at a small number of layers.

The quasi-particle self-consistent *GW* (QSGW)^{37–39} method combined with the self-consistent solution of Bethe-Salpeter equation (BSE), $QSGW\hat{W}$ ^{40–42} is used to calculate the band structure, giving a band gap near 3.6 eV (Figure 1g), where we note that the more common local-density approximation (LDA) provides a significantly different value (0.5 eV). Macroscopic dielectric response is computed incorporating the electron-hole two-particle correlations through higher order Feynman diagrams. The calculated dielectric properties of MnPS₃ offer insight into potential utility in the plasmonic arena. The real and imaginary parts of the dielectric function are presented in figures 1 **h** and **i**, respectively, where the out-of-plane absorption is dramatically different from in-plane absorption. A more detailed comparison of calculations can be found in the supplemental materials.

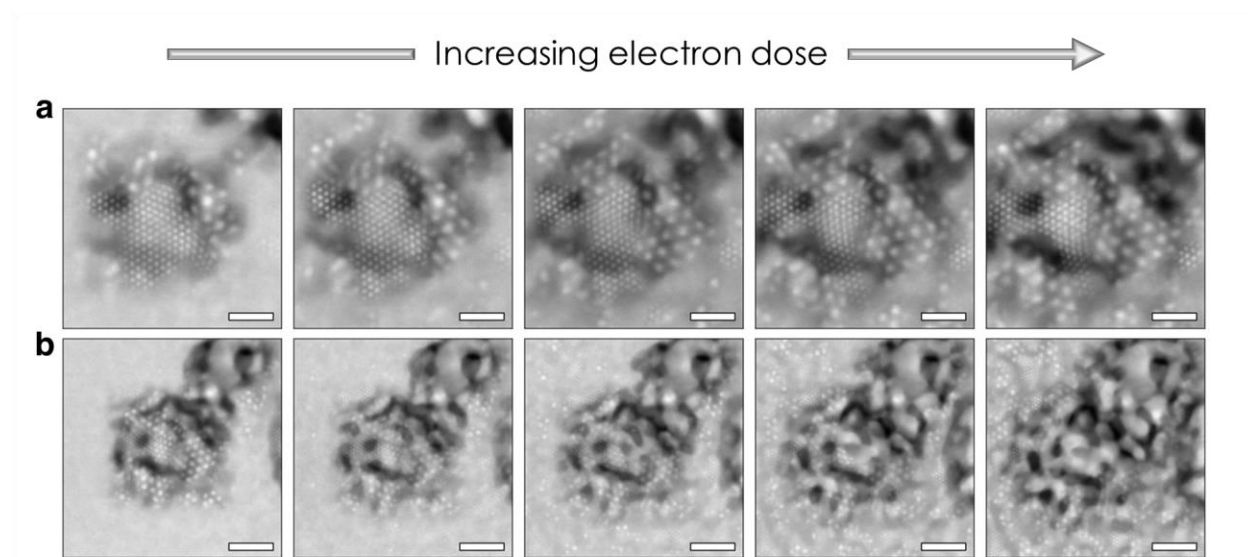


Figure 2. Beam-induced mesoscopic ordering. HAADF-STEM images acquired sequentially with a defocused electron probe showing formation of periodic features on the nanometer scale. Two different fields of view are shown separately in **a** and **b**, where equal time steps are shown. Full-frame videos found in supplementary materials. Scalebars in **a** and **b** are 10 and 20 nm, respectively.

During routine HAADF-STEM imaging, we observe that in several layer MnPS₃, the electron beam begins to modify the structure locally. This modification can include degradation of materials and formation of holes for large exposures, as well as much more subtle changes of atomic structure. Experimentally, we have established that optimal conditions for observation of

this dynamic is to intentionally defocus the converged electron beam on the order of 50 nm and sweep the beam in a field of view of at least several nanometers. Different scan strategies (paths, dwell times, defocus, etc.) were tested, and while most any condition causes these dynamics, the slightly defocused approach appeared to increase the rate of formation of periodic features, we presume because the dose is balanced with the probe size under this defocused condition. In other words, a slightly defocused probe provides enough dose to locally induce changes but not too much to destroy the structure too quickly.

If a large field of view of the specimen is inspected with a moderate imaging duration using the described defocused approach, well-ordered structures start to emerge – these are shown in several time increments in **Figure 2**, with complete videos and tracking of the phases found in the Supplementary materials. One likely will immediately recognize such periodic lattice modulations that are reminiscent of the moiré interference seen in twisted materials in both STM and STEM.^{43,44} We note that several apparent moiré wavelengths appear, and in a way compete with one another leading with rather spectacular dynamic evolution. This remarkably unique beam-induced transformation generates ordered periodic structures on the mesoscopic scale, but questions remain as to what causes the periodic behavior and what properties the modulated structures exhibit.

It is important to note that the formation of these periodic patterns is often followed by significant damage in the material and formation of holes. However, the process can be controlled and stopped at different stages, and often very complex dynamics of a periodically ordered phase is observed prior to the onset of irreversible damage. This observation strongly suggests the potential role of beam-induced stoichiometry changes in the emergence of these structures. We find no such beam induced effects in the sister material MnPSe₃, further strengthening the idea that sulfur removal is largely responsible.

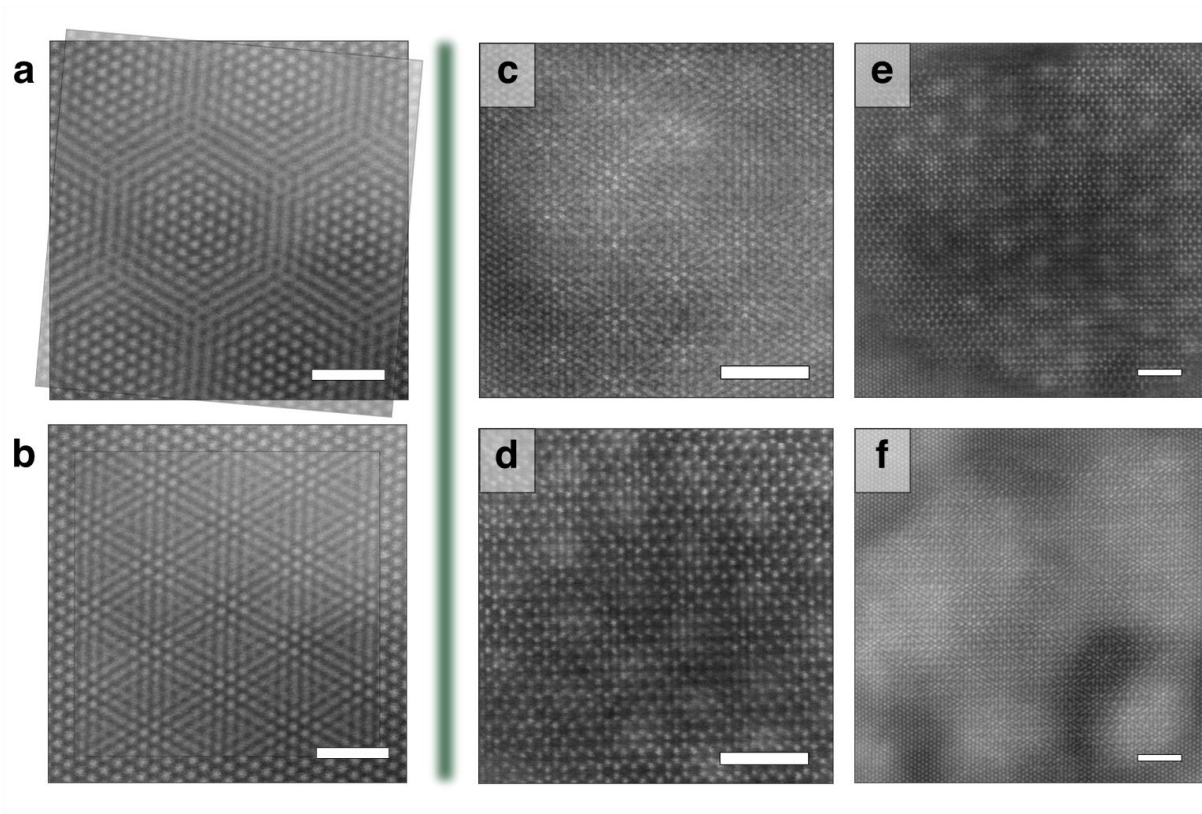


Figure 3. Atomistic mechanisms of mesoscopic ordering. Qualitative scenario for emergence of the structures via synthetic 5° rotation (**a**) and 15% compression (**b**) of one image relative to another. Atomic resolution HAADF-STEM imaging shows presence of periodic nanometer scale features at a variety of number of layers in **c-f**. All scalebars are 2 nm.

We further explore the qualitative origins of the observed contrast after electron irradiation. After the structures have formed, the electron probe is focused, and small fields of view are captured by HAADF-STEM imaging and shown in **Figure 3**. Arguably the most common circumstance which produces moiré superlattices is when one lattice twists relative to another. If this is synthetically done *via* image analysis techniques as shown schematically in Figure 3a, the recognizable moiré features arise in the lattice, but these are distinctly different from what is observed. On the other hand, if one lattice is compressed or expanded relative to the other, a much better qualitative match is seen (Fig 3b). This however is a peculiar notion since the lattice compression of one layer that is needed to realize the same degree of long-range period that is observed is on the order of 15% or higher, which is by no means a small amount. Moreover, the transformation is *local*, suggesting the presence a sharp, strained boundary between the native and compressed regions. At the same time, the local nature of transformations implies the ability to pattern such structures and is evaluated later.

While moiré structures form under electron beam irradiation in the presence of any number of layers more than one, a relationship between number of layers and observable configurations is

seen in the HAADF-STEM images in Figure 3c-f. We find that relatively fewer number of layers produce structures shown in Fig 3e while greater number of layers produce that shown in Fig 3f. Notably, the boundary between the original and newly formed structures is clearly seen in most of the experimental micrographs in Figure 3.

To gain a better understanding of the structure changes, we study the time dynamics of the system under irradiation by collecting stacks of HAADF-STEM images. Both the moiré formation at the mesoscale and the lattice periodicity determined by Fast Fourier Transforms (FFTs) are analyzed at each step. Surprisingly, a large range of periods is observed in the FFT calculated from near the end of the image stack as seen in **Figure 4**, indicating the generation of long-range and short-range periodicity. Emergence of the moiré interference occurs after only a few frames. Multiple moiré phases simultaneously exist – one with ~ 1.35 nm period and another with ~ 1.6 nm period; this is not surprising after seeing a variety of order competition in Figure 2. FFT analysis also shows initial periodicity of 0.3 nm which corresponds to a honeycomb rather than hexagonal lattice, yet this separates into 0.27 nm and 0.34 nm near 20 frames of exposure, suggesting that - in a local environment - one or more layers are stretched in one direction.

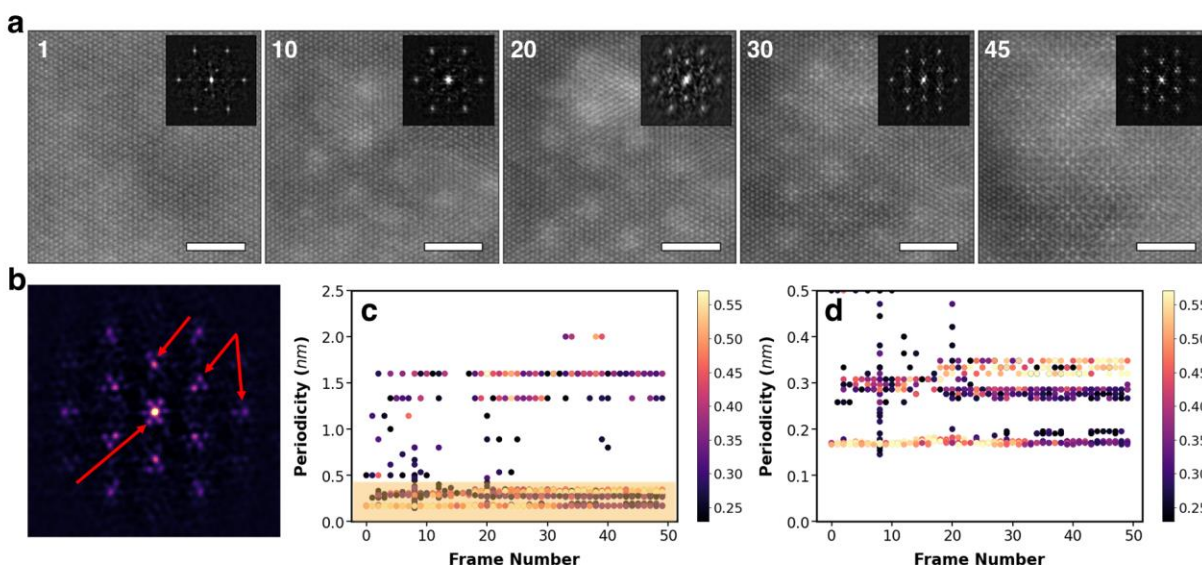


Figure 4. Atomistic time dynamics. HAADF-STEM images at specified time intervals (frame numbers) shown in **a**, with FFT insets, where final frame FFT is enlarged in **b** showing emergence of several superlattice peaks. FFT peaks are detected in each frame and their corresponding real space dimensions are tracked in time in **c**, where the shaded region is blown up in **d**.

Our hypothesized mechanism for the ordered transformation is that the electron beam effectively compresses one layer relative to another by removal of sulfur atoms, producing periodic moiré-like interference – but only where the beam is positioned. Thus, this enables us to generate a new type of structure which fundamentally embraces a new effect - the properties of which are not yet well understood. We posit that the S atoms are more likely to be knocked out from either

the top or bottom layer, or both, such that the internal structure remains intact, but the surfaces are strongly modified.

In order to understand the origin of observed moiré-like interference, we further explore the role of sulfur vacancies in the lattice using density functional theory (DFT) calculations. **Figure 5** shows that in doing so, the Mn atoms do indeed shift relative to their original atomic coordinates, even with a few number of sulfur atoms removed. While DFT was shown to not be accurate for calculating the electronic band structure and dielectric properties, it can on the other hand provide initial insights into the atomic coordinates of the system upon formation of sulfur vacancies.

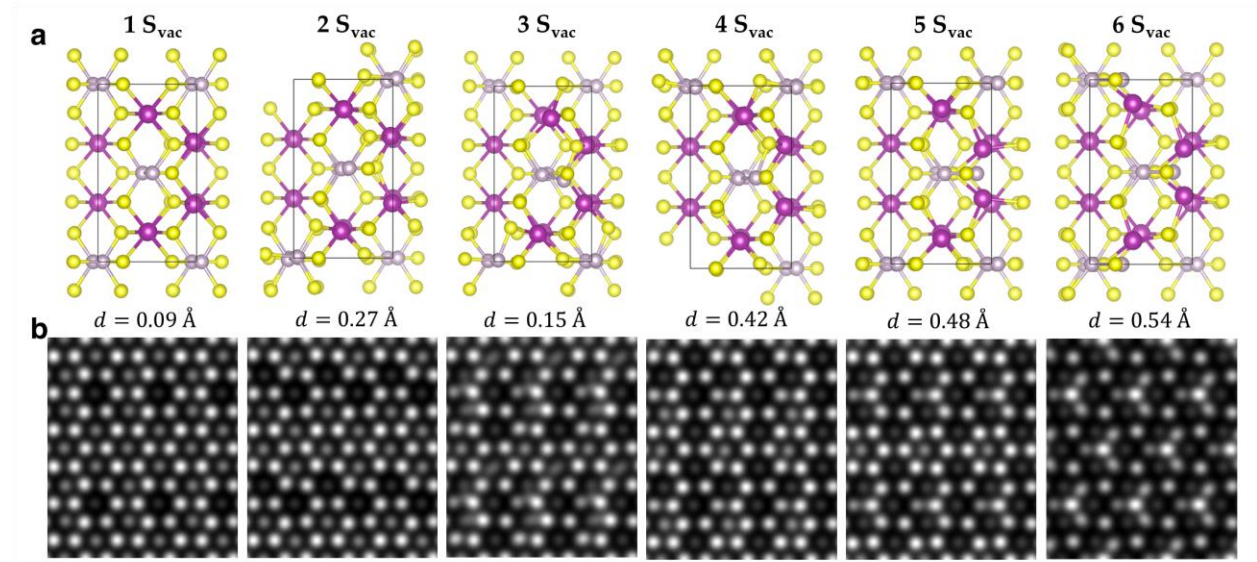


Figure 5. Calculated atomic rearrangements upon sulfur vacancy formation. DFT calculations of two-layer system (a) where top layer incurs different number of sulfur vacancies, where (b) shows HAADF-STEM image simulations of the corresponding two-layer system. Magnitude of largest atomic displacement, d , is provided for each variant.

In the DFT approach, we considered a $MnPS_3$ system of two constituent layers. Systematically, sulfur atoms were removed from the top layer. Several configurations of the S vacancies in the vicinity of the Mn were considered. As the lowest-energy sites occur in the neighborhood of Mn, all possible first and second neighboring S vacancy sites were considered. The side views of the representative model indicating the Mn displacement and S vacancy sites are shown in Figure 5a.

It is evident from Figure 5 that S vacancies result in a displacement in the stacking of the $MnPS_3$ homo-bilayer. This high-symmetry stacking (AA type) corresponds to regions where one Mn atom is eclipsed by another Mn of the opposite layer in each unit cell. Furthermore, with increasing S vacancy concentration, the stacking of Mn atoms in different layers undergoes a relative increasing displacement which results in moiré-like interference. It is also observed that

the displacement of the Mn atoms increases from 0.09 Å (for one S vacancy) to 0.54 Å (full, six-vacancy incorporation). The displacements shown in the six-vacancy schematic agree with our FFT analysis in that the hexagon of Mn atoms (with six S vacancies) undergoes an anisotropic “stretching” that results in apparent superlattice peaks.

We next consider whether this modification can modify the electronic and dielectric properties of the material, as was recently demonstrated in MoS₂/WSe₂ twisted heterostructures,⁴⁵ opening a pathway for feature engineering. In the STEM environment, EELS provides a direct link to the electromagnetic local density of states^{46,47} on the nanometer and even atomic scales. The incident electron energy, here $E_0 = 60kV$, has a probability to transfer a portion of its energy inelastically that leads to an electronic excitation event, where the change in electron energy is detected using a magnetic spectrometer. STEM-EELS allows to probe the local electronic behavior by collecting the EEL spectra at an array of probe positions – this is performed here for both a region of moiré structures and a large encompassing field of view. By nature, the data structure is three dimensional (two of space, one of energy), hence visualization can be non-intuitive. For this reason, non-negative matrix factorization (NMF)⁴⁸ – a spectral decomposition technique that is now common in the electron microscopy and other fields^{49–51} – is chosen to explore the data space and is presented in **Figure 6**.

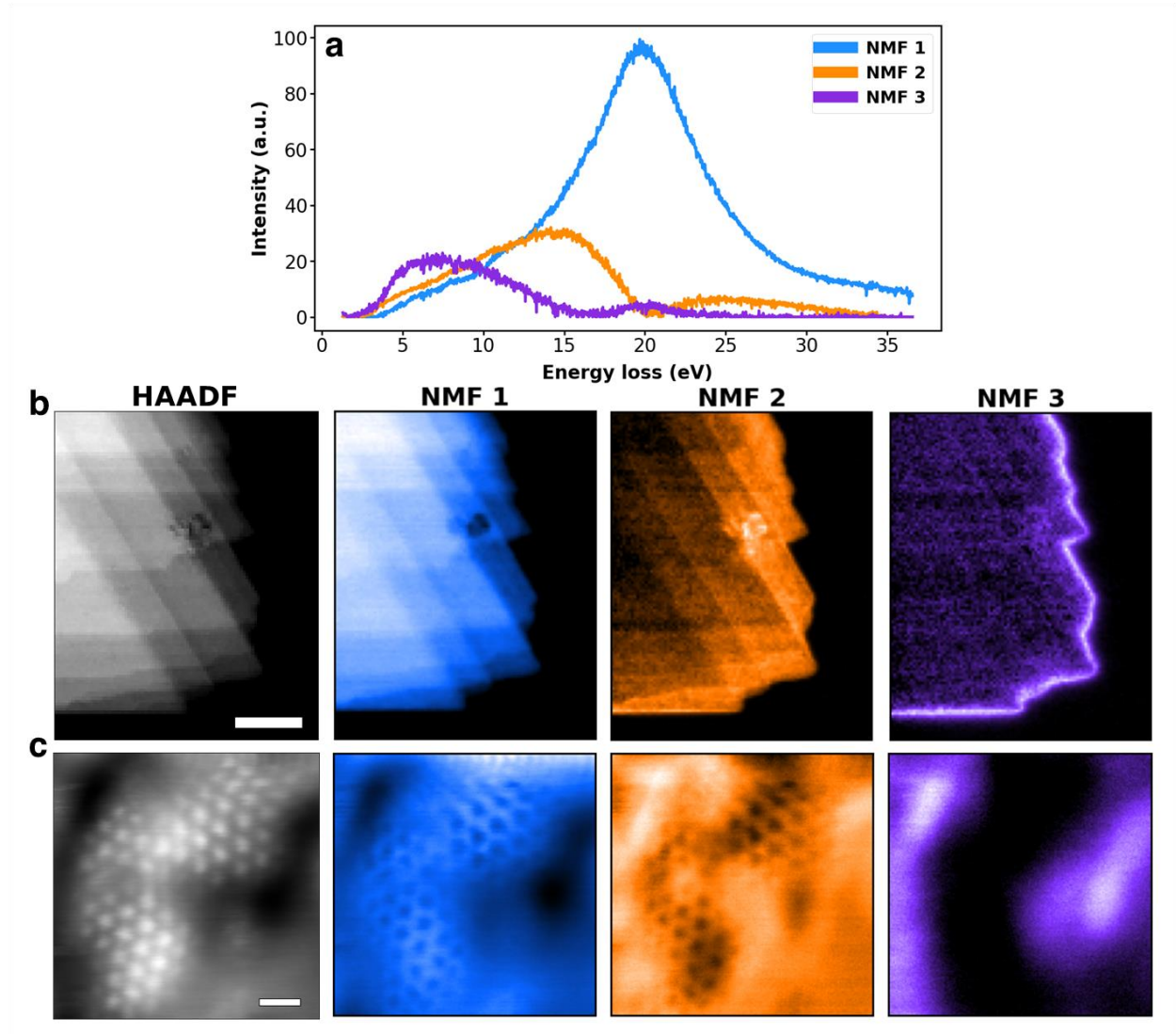


Figure 6. STEM-EELS mapping visualized by NMF decomposition. Large scale native features in panel **b**; electronic behavior arising from moiré features in **c**. Spectral endmembers in **a** are decomposed from data shown in panel **b** by three-component NMF extraction. NMF model from **b** is used to decompose hyperspectral data in **c**. Scalebars in **b** and **c** are 50 nm and 5 nm, respectively.

Examination of a 2D flake on the mesoscopic scale shows several distinct plasmonic features seen in Figure 6a and 6b. We recently discovered the presence of a highly localized edge plasmon in MnPS_3 *via* autonomous active learning;⁵² here, localization and response of this plasmon are clearly seen in the NMF 3 component (purple) whose peak energy lies near 6 eV. The length scale of the edge plasmon is curiously on the same order as the emergent mesoscopic ordering, suggesting the possibility of coupling between the two effects. Next, we inspect the energy loss variations arising within the beam-induced moiré regions, again by using NMF to reveal if there exists any underlying plasmonic discrepancies from formation of the structures.

Edge plasmons are generated as evidenced by NMF 3 component in Figure 6c, which is not surprising given that the electron beam has created a new edge by removal of some material. The bulk resonance reduces in energy with decreasing number of layers and can be used as a fingerprint in thickness determination.²² In this way, NMF generally separates thin from thick regions which is clearly seen in Figure 6b (NMF 1 and NMF 2). A subtle change manifests in the plasmon resonance near 15 eV (Fig. 6c, NMF 2) where the relative intensity decreases in the moiré regions and increases immediately outside them, in contrast to the resonance near 20 eV which behaves as expected where the intensity reduces for thinner regions and is constant otherwise. This suggests that there is indeed a change to the local plasmon response upon mesoscopic ordering and with further study could be a basis for coupling to edge modes.

Finally, the feasibility of locally patterning the mesoscopically ordered structures is evaluated in **Figure 7**. Edge engineering⁶ in transition metal dichalcogenides using the electron beam in the STEM has been ongoing for several years, hence we envision patterning of MnPS₃ and possibly other metal phosphorous trichalcogenides to complement these efforts. Initial testing of simple rectangular shapes directly utilizing rectangular sub-scans yields the structures seen in Figure 7a. Taking this a step further we realized more sophisticated patterns can be generated, such as the laboratory logo seen in Figure 7b. Even here, several different moiré phases have emerged. Automating the formation of these structures is therefore critical, and while we show the first steps towards this goal, implementation of feedback into the patterning routines undoubtedly will lead to more precise structures, increased reproducibility, and targeted functionalities.

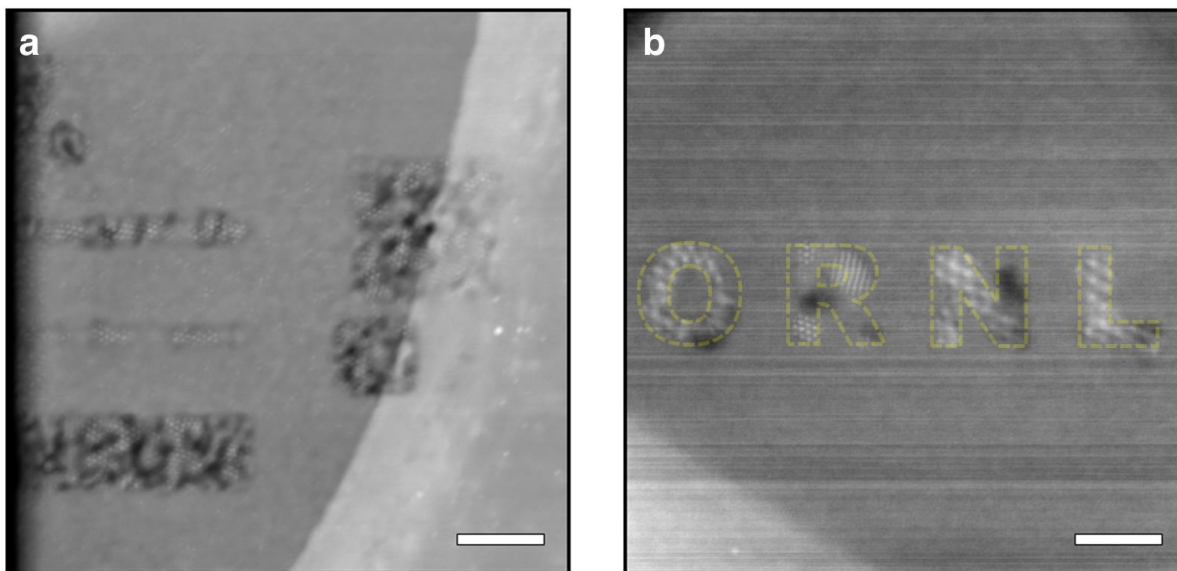


Figure 7. Patterning of mesoscopic ordered phenomena. Simple rectangular features in **a**; more complex shapes in **b**. Scale bars in **a** and **b** are 50 and 20 nm.

To summarize, we report highly unusual structural reconstructions in layered MnPS₃ associated with the emergence of the distinct mesoscale periodicities. Unlike the twisted structures,

in this case the mechanism seems to be associated with the expansion/contraction of individual layers, the behavior we attribute to beam-induced stoichiometry changes. Remarkably, these behaviors are induced and control by the electron beam, demonstrating a broad range of dynamic behaviors resembling the nucleation and growth of new phases, and opening a new pathway for selective control of matter on the atomic scales. We further explore the evolution of the plasmonic properties induced by the formation of these ordered structures.

These findings open the pathway to the fundamentally new paradigm towards engineering the electronic and quantum properties locally, using the MnPS_3 and similar materials as a beam-controlled component. The fact that the many stacking patterns in the metal phosphorous trichalcogenide materials are nearly iso-energetic leads us to speculate that such effects may also occur in other metal phosphorous trichalcogenide compounds (those with sulfur) allowing for an even greater number of beam-engineerable materials waiting to be discovered. Recent progress in autonomous microscopy⁵² and other automated experiments⁵³ may provide exactly this pathway. These materials coupled with beam engineering are promising candidates for beyond CMOS devices.

Acknowledgements: This effort (electron microscopy) is based upon work supported by the U.S. Department of Energy (DOE), Office of Science, Basic Energy Sciences (BES), Materials Sciences and Engineering Division (K.M.R., S.V.K.) and was performed and partially supported at the Oak Ridge National Laboratory's Center for Nanophase Materials Sciences (CNMS), a U.S. Department of Energy, Office of Science User Facility. This research used resources of the Compute and Data Environment for Science (CADES) at the Oak Ridge National Laboratory, which is supported by the Office of Science of the U.S. Department of Energy under Contract No. DE-AC05-00OR22725. V.S. acknowledges the XSEDE allocation (Grant No. TG- DMR200008) and the Infrastructure for Scientific Applications and Advanced Computing (ISAAC) at the University of Tennessee for the computational resources. Research at the University of Tennessee is supported by the U.S. DOE, BES, Materials Science Division under award DE-FG02-01ER45885 (J.L.M.). N.H. and D.M. were supported by the National Science Foundation through grant number DMR-1808964. MIK and SA are supported by the ERC Synergy Grant, project 854843 FASTCORR (Ultrafast dynamics of correlated electrons in solids). DP is supported by the National Renewable Energy Laboratories. SA, DP and MIK acknowledge PRACE for awarding us access to Juwels Booster and Cluster, Germany.

Materials and methods

Growth and exfoliation

MnPS₃ single crystals were synthesized through the chemical vapor transport (CVT) method. Manganese powder (Alfa Aesar 99.95%), phosphorus powder (Alfa Aesar 99.995%) and sulfur chunks (Puratronic 99.9995%) of a ratio 1: 1: 3.1 were thoroughly mixed and ground under argon atmosphere. The mixture was then pressed into a pellet and sealed in a fused tube under vacuum. Polycrystalline powder was obtained after annealing the ampoule in a muffle furnace for one week at 730°C. 2 grams of annealed powder was transferred into a new fused tube. Dehydrated iodine was added as a transport agent. The tube was then connected to a vacuum station and sealed at a proper length. Large single crystal could be harvested at the cold end of the tube after annealing at 700°C for 6 days in a tube furnace.

Samples for electron microscopy were prepared using standard mechanical exfoliation techniques where flakes were directly exfoliated onto Au Quantifoil grids using thermal release tape, skipping transfer steps to and from silicon which eliminates any chemical processes. Only sheets suspended over perforated holes in the membrane were inspected.

Electron microscopy

Microscopy was performed using a NION monochromated fifth order aberration corrected scanning transmission electron microscope (MACSTEM). An accelerating voltage of 60 kV with nominal probe current of 20 pA was used in the experiments. Pressure at the sample was kept at 10⁻⁹ Torr or better. Convergence semi-angle was set to 30 mrad.

Image simulations

All simulations were performed using the quantum excitation of phonons option in the μ STEM package.³⁶ The unit cells were tiled to for a supercell of approximately 3nm by 3 nm and 1024 pixels were used in each direction. An aberration free probe with an aperture of 30 mrad with an energy of 60keV was used. A total of 80 phase gratings were calculated, resulting in a total of 1200 distinct phase grates due to phase ramp shifting of the potentials. Eight passes through the sample were used in all cases. An annular ADF detector with a 61 mrad inner angle and a 300 mrad outer angle were used. To account for temporal incoherence a focal series of 21 images were calculated covering a range of 10 nm with side of zero defocus. Assuming a chromatic aberration coefficient of $C_c = 1.3mm$ and a Gaussian energy spread with a fullwidth half maximum (FWHM) of 0.35 eV, the weighted average image was calculated. To account for source size effects, the images were blurred with a Gaussian with a FWHM of 0.075 nm.

Density functional theory

The DFT calculations were performed using the Vienna *ab initio* simulation package (VASP) code, using the Perdew–Burke–Ernzerhof (PBE)³⁶ generalized gradient approximation (GGA), the projector-augmented wave approach, and a cutoff energy of 500 eV for the plane wave expansion of the wave functions. Geometries were relaxed using a conjugate gradient algorithm until the forces on all unconstrained atoms became smaller than < 0.03 eV/Å. Appropriate Monkhorst-Pack k-point meshes were considered to produce results with an energy convergence of 0.5 meV/atom.

QSGW theory

The quasi-particle self-consistent GW (QSGW) method^{37–39} is an approach to find an optimal starting point independent, ab-initio independent-particle Hamiltonian self-consistently within the GW approximation to the self-energy (Σ). The QSGW^{40–42} method additionally includes vertex corrections in the polarizability (precursor to the effective interaction W) by solving the Bethe-Salpeter equation (BSE) for the two-particle Hamiltonian in each self-consistency cycle.

The crucial difference in our implementation of QSGW from most other implementations of BSE is that our calculations are self-consistent in both self energy Σ and the charge density.^{42,54} W is calculated with ladder-BSE corrections and the self energy, using a static vertex in the BSE. G , Σ and W are updated iteratively until all of them converge. Brillouin zone (BZ) sampling for single particle quantities (density and energy bands with the static quasiparticlized QSGW self-energy $\Sigma^0(k)$) used a $6 \times 6 \times 4$ origin centered mesh while the (relatively smooth) dynamical self-energy $\Sigma(k)$ was constructed using a $3 \times 3 \times 2$ k-mesh using the Γ offset points method and $\Sigma^0(k)$ extracted from it. For each iteration in the QSGW self-consistency cycle, the charge density was made self-consistent. The QSGW cycle was iterated until the RMS change in Σ^0 reached 10^{-5} Ry. Thus the calculation was self-consistent in both $\Sigma^0(k)$ and the density. Numerous checks were made to verify that the self-consistent $\Sigma^0(k)$ was independent of starting point, for both QSGW and QSGW calculations; e.g. using LDA or Hartree-Fock self-energy as the initial self energy for QSGW and using LDA or QSGW as the initial self-energy for QSGW. LDA underestimates the electronic correlations severely in MnPS₃ and predicts a band gap of 0.5 eV, QSGW enhances the gap to 4 eV and ladders in QSGW screens the W to reduce the gap to 3.6 eV. We check convergence in the QSGW band gap and macroscopic dielectric response by increasing the size of the two-particle Hamiltonian. We find that they converge with 60 valence bands and 48 conduction bands. Excitons with positive binding energies ~ 0.7 eV are observed in the vertex corrected optical spectrum. For our simulations we used the crystal structure id-8613 in materialsproject.org.

Data availability

Electron microscopy data and analysis codes are freely available here: <https://git.io/JaCCz>

All the input file structures and the commandlines to launch calculations are rigorously explained in the tutorials available on the Questaal webpage.⁵⁵ The source codes for LDA, QSGW and QSGW are available from Ref[55] under the terms of the AGPLv3 license.

References

1. Krivanek, O. L., Lovejoy, T. C., Dellby, N. & Carpenter, R. W. Monochromated STEM with a 30 meV-wide, atom-sized electron probe. *Microscopy (Oxf)* **62**, 3–21 (2013).
2. Hachtel, J. A., Lupini, A. R. & Idrobo, J. C. Exploring the capabilities of monochromated electron energy loss spectroscopy in the infrared regime. *Scientific Reports* **8**, 5637 (2018).
3. Ophus, C. Four-Dimensional Scanning Transmission Electron Microscopy (4D-STEM): From Scanning Nanodiffraction to Ptychography and Beyond. *Microscopy and Microanalysis* **25**, 563–582 (2019).
4. Yang, H. *et al.* 4D STEM: High efficiency phase contrast imaging using a fast pixelated detector. *J. Phys.: Conf. Ser.* **644**, 012032 (2015).
5. Mukherjee, D., Gamler, J. T. L., Skrabalak, S. E. & Unocic, R. R. Lattice Strain Measurement of Core@Shell Electrocatalysts with 4D Scanning Transmission Electron Microscopy Nanobeam Electron Diffraction. *ACS Catal.* **10**, 5529–5541 (2020).
6. Sang, X. *et al.* In situ edge engineering in two-dimensional transition metal dichalcogenides. *Nat Commun* **9**, 2051 (2018).
7. Lin, J. *et al.* Flexible metallic nanowires with self-adaptive contacts to semiconducting transition-metal dichalcogenide monolayers. *Nature Nanotech* **9**, 436–442 (2014).
8. Dyck, O., Kim, S., Kalinin, S. V. & Jesse, S. Placing single atoms in graphene with a scanning transmission electron microscope. *Appl. Phys. Lett.* **111**, 113104 (2017).
9. Tripathi, M. *et al.* Electron-Beam Manipulation of Silicon Dopants in Graphene. *Nano Lett.* **18**, 5319–5323 (2018).
10. Luo, Y. *et al.* In situ nanoscale imaging of moiré superlattices in twisted van der Waals heterostructures. *Nat Commun* **11**, 4209 (2020).
11. Cao, Y. *et al.* Unconventional superconductivity in magic-angle graphene superlattices. *Nature* **556**, 43–50 (2018).

12. Yankowitz, M. *et al.* Tuning superconductivity in twisted bilayer graphene. *Science* **363**, 1059–1064 (2019).
13. Lopez-Bezanilla, A. & Lado, J. L. Electrical band flattening, valley flux, and superconductivity in twisted trilayer graphene. *Phys. Rev. Research* **2**, 033357 (2020).
14. Park, J. M., Cao, Y., Watanabe, K., Taniguchi, T. & Jarillo-Herrero, P. Tunable strongly coupled superconductivity in magic-angle twisted trilayer graphene. *Nature* **590**, 249–255 (2021).
15. Zheng, Z. *et al.* Unconventional ferroelectricity in moiré heterostructures. *Nature* **588**, 71–76 (2020).
16. Kim, C.-J. *et al.* Stacking Order Dependent Second Harmonic Generation and Topological Defects in h-BN Bilayers. *Nano Lett.* **13**, 5660–5665 (2013).
17. Alden, J. S. *et al.* Strain solitons and topological defects in bilayer graphene. *PNAS* **110**, 11256–11260 (2013).
18. Guo, J. *et al.* Topological Defects: Origin of Nanopores and Enhanced Adsorption Performance in Nanoporous Carbon. *Small* **8**, 3283–3288 (2012).
19. Susner, M. A., Chyasnachyus, M., McGuire, M. A., Ganesh, P. & Maksymovych, P. Metal Thio- and Selenophosphates as Multifunctional van der Waals Layered Materials. *Advanced Materials* **29**, 1602852 (2017).
20. Wang, F. *et al.* New Frontiers on van der Waals Layered Metal Phosphorous Trichalcogenides. *Advanced Functional Materials* **28**, 1802151 (2018).
21. Ohno, Y. Systematic study of layered metal-phosphor-trisulfides MPS_3 ($\text{M} = \text{Mg}, \text{Mn}, \text{Fe}, \text{Ni}, \text{Zn}, \text{Cd}$). *Solid State Communications* **67**, 1089–1092 (1988).
22. Kinyanjui, M. K., Koester, J., Boucher, F., Wildes, A. & Kaiser, U. Spectroscopic properties of a freestanding MnPS_3 single layer. *Phys. Rev. B* **98**, 035417 (2018).
23. Luong, D. H., Phan, T. L., Ghimire, G., Duong, D. L. & Lee, Y. H. Revealing antiferromagnetic transition of van der Waals MnPS_3 via vertical tunneling electrical resistance measurement. *APL Materials* **7**, 081102 (2019).

24. Sun, Y.-J., Tan, Q.-H., Liu, X.-L., Gao, Y.-F. & Zhang, J. Probing the Magnetic Ordering of Antiferromagnetic MnPS₃ by Raman Spectroscopy. *J. Phys. Chem. Lett.* **10**, 3087–3093 (2019).
25. Kim, K. *et al.* Antiferromagnetic ordering in van der Waals 2D magnetic material MnPS₃ probed by Raman spectroscopy. *2D Mater.* **6**, 041001 (2019).
26. Long, G. *et al.* Persistence of Magnetism in Atomically Thin MnPS₃ Crystals. *Nano Lett.* **20**, 2452–2459 (2020).
27. Kumar, R., Jenjeti, R. N., Austeria, M. P. & Sampath, S. Bulk and few-layer MnPS₃: a new candidate for field effect transistors and UV photodetectors. *J. Mater. Chem. C* **7**, 324–329 (2019).
28. Kumar, R., Jenjeti, R. N. & Sampath, S. Two-Dimensional, Few-Layer MnPS₃ for Selective NO₂ Gas Sensing under Ambient Conditions. *ACS Sens.* **5**, 404–411 (2020).
29. Silipigni, L., Schirò, L., Monsù Scolaro, L., De Luca, G. & Salvato, G. Lithium ions conduction in Li₂Mn_{1-x}PS₃ films. *Philosophical Magazine* **94**, 4026–4036 (2014).
30. Neal, S. N. *et al.* Near-field infrared spectroscopy of monolayer MnPS₃. *Phys. Rev. B* **100**, 075428 (2019).
31. Neal, S. N. *et al.* Symmetry crossover in layered MPS₃ complexes (*M*=Mn, Fe, Ni) via near-field infrared spectroscopy. *Phys. Rev. B* **102**, 085408 (2020).
32. Harms, N. C. *et al.* Piezochromism in the magnetic chalcogenide MnPS₃. *npj Quantum Mater.* **5**, 1–7 (2020).
33. Egerton, R. F. Mechanisms of radiation damage in beam-sensitive specimens, for TEM accelerating voltages between 10 and 300 kV. *Microscopy Research and Technique* **75**, 1550–1556 (2012).
34. Egerton, R. F. Control of radiation damage in the TEM. *Ultramicroscopy* **127**, 100–108 (2013).
35. Nitsche, R. & Wild, P. Crystal growth of metal-phosphorus-sulfur compounds by vapor transport. *Materials Research Bulletin* **5**, 419–423 (1970).
36. Allen, L. J., D'Alfonso, A. J. & Findlay, S. D. Modelling the inelastic scattering of fast electrons. *Ultramicroscopy* **151**, 11–22 (2015).

37. van Schilfgaarde, M., Kotani, T. & Faleev, S. Quasiparticle Self-Consistent GW Theory. *Phys. Rev. Lett.* **96**, 226402 (2006).
38. Kotani, T., van Schilfgaarde, M. & Faleev, S. V. Quasiparticle self-consistent GW method: A basis for the independent-particle approximation. *Phys. Rev. B* **76**, 165106 (2007).
39. Pashov, D. *et al.* Questaal: A package of electronic structure methods based on the linear muffin-tin orbital technique. *Computer Physics Communications* **249**, 107065 (2020).
40. Cunningham, B., Gruening, M., Pashov, D. & van Schilfgaarde, M. QSGW: Quasiparticle Self consistent GW with ladder diagrams in W. *arXiv:2106.05759 [cond-mat]* (2021).
41. Cunningham, B., Gruening, M., Azarhoosh, P., Pashov, D. & van Schilfgaarde, M. Effect of ladder diagrams on optical absorption spectra in a quasiparticle self-consistent GW framework. *Physical Review Materials* **2**, (2018).
42. Acharya, S. *et al.* Electronic Structure of Chromium Trihalides beyond Density Functional Theory. *arXiv:2106.06564 [cond-mat]* (2021).
43. Kerelsky, A. *et al.* Maximized electron interactions at the magic angle in twisted bilayer graphene. *Nature* **572**, 95–100 (2019).
44. Weston, A. *et al.* Atomic reconstruction in twisted bilayers of transition metal dichalcogenides. *Nat. Nanotechnol.* **15**, 592–597 (2020).
45. Susarla, S. *et al.* Mapping Modified Electronic Levels in the Moiré Patterns in MoS₂/WSe₂ Using Low-Loss EELS. *Nano Lett.* **21**, 4071–4077 (2021).
46. García de Abajo, F. J. & Kociak, M. Probing the Photonic Local Density of States with Electron Energy Loss Spectroscopy. *Phys. Rev. Lett.* **100**, 106804 (2008).
47. Bigelow, N. W., Vashillo, A., Iberi, V., Camden, J. P. & Masiello, D. J. Characterization of the Electron- and Photon-Driven Plasmonic Excitations of Metal Nanorods. *ACS Nano* **6**, 7497–7504 (2012).
48. Lee, D. D. & Seung, H. S. Learning the parts of objects by non-negative matrix factorization. *Nature* **401**, 788–791 (1999).

49. Shiga, M. *et al.* Sparse modeling of EELS and EDX spectral imaging data by nonnegative matrix factorization. *Ultramicroscopy* **170**, 43–59 (2016).
50. Zhang, S. & Scheu, C. Evaluation of EELS spectrum imaging data by spectral components and factors from multivariate analysis. *Microscopy* **67**, i133–i141 (2018).
51. Agrawal, A. *et al.* Resonant Coupling between Molecular Vibrations and Localized Surface Plasmon Resonance of Faceted Metal Oxide Nanocrystals. *Nano Lett.* **17**, 2611–2620 (2017).
52. Roccapriore, K. M., Kalinin, S. V. & Ziatdinov, M. Physics discovery in nanoplasmonic systems via autonomous experiments in Scanning Transmission Electron Microscopy. *arXiv:2108.03290 [cond-mat, physics:physics]* (2021).
53. Doty, C. *et al.* Design of a Graphical User Interface for Few-Shot Machine Learning Classification of Electron Microscopy Data. *arXiv:2107.10387 [cond-mat]* (2021).
54. Ismail-Beigi, S. Justifying quasiparticle self-consistent schemes via gradient optimization in Baym–Kadanoff theory. *J. Phys.: Condens. Matter* **29**, 385501 (2017).
55. Questaal Home. <https://www.questaal.org/>.